

Atomic Ru catalysis for ethanol coupling to C₄₊ alcoholsBowen Yuan^a, Jian Zhang^{a,*}, Zhe An^a, Yanru Zhu^a, Xin Shu^a, Hongyan Song^a, Xu Xiang^a, Wanning Wang^a, Yusheng Jing^a, Lirong Zheng^{b,*}, Jing He^{a,*}^a State Key Laboratory of Chemical Resource Engineering & Beijing Advanced Innovation Center for Soft Matter Science and Engineering, Beijing University of Chemical Technology, Beijing 100029, PR China^b Institute of High Energy Physics, The Chinese Academy of Sciences, Beijing 100049, PR China

ARTICLE INFO

Keywords:

Ethanol

Coupling reaction

C₄₊ alcohols

Layered double oxides

Atomic Ru

ABSTRACT

Transformation of ethanol to more valuable C₄₊ alcohols by coupling reaction has been of great interest from the point of view of chemistry and technology of biomass utilization. This work reports atomic Ru on Mg and Al containing layered double oxides (MgAl-LDO) for ethanol coupling to C₄₊ alcohols. The atomic Ru remarkably promotes the coupling of ethanol, achieving a selectivity of 82.6% to C₄₊ alcohols under an ethanol conversion of 29.6%. Through tailoring Ru dispersion and acid-base properties, it has been found that atomic Ru promotes ethanol dehydrogenation and the following aldol condensation of acetaldehyde.

1. Introduction

Air pollution is one of the major environmental problems in the world, because it is the main cause of human respiratory diseases. In recent decades, the world has been paying attention to the problem of automobile exhaust emission. Automobile exhaust, such as carbon monoxide, sulfur dioxide and other harmful gases, has caused great pressure on the atmospheric environment. Therefore, governments all over the world attach great importance to improving fuel quality and recommend using ethanol and butanol as blending components of gasoline to improve fuel quality and reduce the emission level of harmful gases. Ethanol, an important biomass-based platform molecule, has been used as the most common blending component of gasoline for light vehicles. Ethanol has high octane number and good explosion resistance. Compared to ethanol, n-butanol has higher energy density (29 MJ/L, about 90% to that of gasoline, higher 21 MJ/L of ethanol), lower moisture absorption, and lower corrosion properties [1,2]. Therefore, n-butanol is considered to be a more ideal blending component of gasoline than ethanol.

The coupling of ethanol is a significant process to produce C₄₊ alcohols including n-butanol and higher alcohols [3]. For n-butanol, it can not only be used as blending component of gasoline, but also be used as a feed stock for the synthesis of plasticizer dibutyl terephthalate, polymer monomer butyl acrylate, or defoaming agent tributyl phosphate; For higher alcohols, they can be used to prepare surfactants (Bayer CropScience) [4]. C₄₊ alcohols have so far been produced mainly through the

hydroformylation process of alkenes under high pressure [5]. Alternatively, ethanol coupling offers a mild and facile route for C₄₊ alcohol production, attracting extensive attention from researchers [3].

Ethanol coupling has been proposed to follow two mechanisms, i.e., Guerbet reaction via aldehyde as intermediate or direct coupling reaction of one ethanol with a second by dehydration [3]. The Guerbet reaction via aldehyde as intermediate is a multi-step tandem reaction, consisting of dehydrogenation of ethanol to acetaldehyde, aldol condensation of two acetaldehyde molecules, dehydration of the aldolization product, and subsequent hydrogen transfer to form saturated alcohols. Each step could be accompanied by competitive side-reaction. Such a complicated process for ethanol coupling to butanol hence brings a great challenge to catalyst and catalytic system. The catalytic system for the alcohol coupling by C-C addition was first investigated in 1899, as Marcel Guerbet reported that n-butanol can be transformed into 2-ethylhexan-1-ol by the presence of metal alkoxides under heating. The coupling of ethanol to C₄₊ alcohols via either homogeneous or heterogeneous catalytic process has been reported by many researchers. In the homogeneous catalytic process, more than 90% selectivity of C₄₊ alcohols (e.g., C₄-C₁₂) can be obtained by using Ru [6–11], Ir [12–14], or Mn [15] complex as catalysts, combined with sodium ethoxide or other strong bases. But in the heterogeneous catalytic process, ethanol coupling to C₄₊ alcohols is more challenging, because the competitive side-reactions, such as ethanol dehydration to diethyl ether or ethylene, one-step esterification to ethyl acetate, and/or Lebedev reaction to 1,3-butadiene [16], are more liable to accompany. Such heterogeneous

* Corresponding authors.

E-mail addresses: zhangjian450924@mail.buct.edu.cn (J. Zhang), zhenglr@ihep.ac.cn (L. Zheng), jinghe@263.net.cn (J. He).<https://doi.org/10.1016/j.apcatb.2022.121271>

Received 31 December 2021; Received in revised form 24 February 2022; Accepted 28 February 2022

Available online 2 March 2022

0926-3373/© 2022 Elsevier B.V. All rights reserved.

catalysts as MgO [17], basic zeolites [18], acid-base bifunctional metal oxides [19,20], hydroxyapatite [21–24], and supported transition metals [25–32] have been developed for ethanol coupling to C_{4+} alcohols. Introduction of metal sites have been widely applied to enhanced ethanol dehydrogenation on metal sites under mild conditions [33,34]. Li et al. reported Cu–CeO₂/AC (activated carbon) for ethanol coupling, achieving a selectivity of up to 55.2% to n-butanol with an ethanol conversion of 39.1% by using a fix-bed reactor at 523 K and 2 MPa N₂ [26]. They also reported multifunctional Pd@UiO-66 for ethanol coupling, exhibiting a selectivity of 48.6% to n-butanol with an ethanol conversion of 49.8% by using a fix-bed reactor at 523 K and 2 MPa N₂ [29]. Zhang et al. reported Ni–MgAlO for ethanol coupling, exhibiting a selectivity of up to 55.2% to n-butanol and a selectivity of about 80% to total C_{4+} alcohols with an ethanol conversion of 18.8% by using a fix-bed reactor at 523 K and 3 MPa N₂ [30]. Our group reported Ag particles supported on Mg and Al containing layered double oxides (MgAl-LDO) for ethanol coupling, and a selectivity of up to 76.6% to n-butanol with ethanol STC (site time conversion) of 2200.8 h^{−1} has been achieved on Ag/Mg₂Al-LDO [31]. Ordóñez et al. reported Ru nanoparticles supported on MgAl-LDO has shown very promising 1-butanol productivities in the ethanol coupling reaction, with about 600 μmol·g^{−1}·ks^{−1} of n-butanol productivity obtained [32].

Homogeneous Ru catalyst has been widely applied in the hydrogen transfer reaction [6–11], due to its moderate adsorption energy for hydrogen [35]. This work reports an atomic Ru catalysis for ethanol coupling, building a bridge between homogeneous and heterogeneous Ru catalysis. Atomic Ru has been demonstrated playing an important role in ethanol dehydrogenation and acetaldehyde condensation, due to the unique Ru–O four-coordinated active center, affording a selectivity of 82.6% to C_{4+} alcohols under an ethanol conversion of 29.6%.

2. Experimental section

2.1. Materials

Mg(NO₃)₂·6H₂O, Al(NO₃)₃·9H₂O, NaOH, Na₂CO₃, Zr(NO₃)₄·5H₂O, and Ga(NO₃)₃·xH₂O are all of analytical grade, purchased from Sino-pharm Chemical Reagent Co., Ltd. (Shanghai, China). RuCl₃·xH₂O (Ru 37–40 wt%), K₂RuCl₅·xH₂O (Ru 26–30 wt%), and HPLC-grade ethanol were purchased from Aladdin (Shanghai, China). All chemicals were used as received without further purification. Deionized water was used in all experimental processes.

2.2. Preparation

2.2.1. LDHs

MgAl-LDHs with Mg/Al molar ratio 3 (Mg₃Al₁-LDHs) was synthesized by the co-precipitation method [36]. Typically, a salt solution of Mg(NO₃)₂·6H₂O (56.25 mmol) and Al(NO₃)₃·9H₂O (18.75 mmol) dissolved in 200 mL of deionized water and a solution of NaOH (160 mmol) dissolved in 200 mL of deionized water were simultaneously added drop-wise into a three-necked flask containing a solution of Na₂CO₃ (12.5 mmol) dissolved in 200 mL of deionized water under vigorous stirring with the pH value controlled at 10.0 ± 0.1. The resulting white suspension was aged at 70 °C for 12 h under gentle stirring. The white precipitant was filtrated, washed with deionized water and 95% ethanol until the filtrate was neutral, and dried at 60 °C for 12 h. Mg₃Al_{0.9}Ga_{0.1}-LDHs and Mg₃Al_{0.9}Zr_{0.1}-LDHs were prepared by the same procedure. For the preparation of Mg₃Al_{0.9}Ga_{0.1}-LDHs, the salt solution was adjusted to Mg(NO₃)₂·6H₂O (56.25 mmol), Al(NO₃)₃·9H₂O (16.875 mmol), and Ga(NO₃)₃·xH₂O (1.875 mmol) dissolved in 200 mL of deionized water. For the preparation of Mg₃Al_{0.9}Zr_{0.1}-LDHs, the salt solution was adjusted to Mg(NO₃)₂·6H₂O (56.25 mmol), Al(NO₃)₃·9H₂O (16.875 mmol), and Zr(NO₃)₄·5H₂O (1.875 mmol) dissolved in 200 mL of deionized water.

2.2.2. Ru (III) loading

The Ru loading on LDHs was carried out by pH-controlled deposition (suffixed with P), precipitation deposition (suffixed with D) [37], electrostatic adsorption (suffixed with E), and incipient wetness impregnation (suffixed with I).

Ru(OH)₆^{3−}/Mg₃Al₁-LDHs-P was prepared as follows: 3.0 g of Mg₃Al₁-LDHs was dispersed into 500 mL of deionized water under magnetic stirring (400 rpm) and 1.0 mol/L NaOH was added drop by drop to adjust the pH to 10.5. Meanwhile, 65 mg of RuCl₃·xH₂O was dissolved into 300 mL of deionized water to get a dark brown solution, and then 15 mL of 1.0 M NaOH was added. The resulting solution was filtered through a membrane to remove insoluble impurities, obtaining a clear bright green Ru(OH)₆^{3−}-containing solution. Then the Ru(OH)₆^{3−}-containing solution was added dropwise into the Mg₃Al₁-LDHs suspension under magnetic stirring (400 rpm) at 50 °C. The resulting suspension was maintained at 50 °C for 6 h under magnetic stirring (400 rpm). The resulting dark grey slurry was filtered. The solid was washed with deionized water and 95% ethanol until the filtrate was neutral, and dried under vacuum in an oven at 40 °C for 12 h. Ru(OH)₆^{3−}/Mg₃Al_{0.9}Ga_{0.1}-LDHs-P or Ru(OH)₆^{3−}/Mg₃Al_{0.9}Zr_{0.1}-LDHs-P were prepared by following the same procedures.

Ru(OH)₆^{3−}/Mg₃Al₁-LDHs-D was prepared as follows: 65 mg of RuCl₃·xH₂O was dissolved into 300 mL of deionized water to get a dark brown solution, and then 15 mL of 1.0 M NaOH was added. The resulting solution was filtered through a membrane to remove insoluble impurities, obtaining a clear bright green Ru(OH)₆^{3−}-containing solution. Then 3.0 g of Mg₃Al₁-LDHs was poured into the Ru(OH)₆^{3−}-containing solution and the resulting suspension (pH = 8.5) was maintained at 50 °C for 6 h under magnetic stirring (400 rpm). The resulting dark grey slurry was filtered. The solid was washed with deionized water and 95% ethanol until the filtrate was neutral, and dried under vacuum in an oven at 40 °C for 12 h.

Ru(OH)_x/Mg₃Al₁-LDHs-E was prepared as follows: 106 mg of K₂RuCl₅·xH₂O was dissolved into 300 mL of deionized water to get a dark brown solution, and then 30 mL of 0.1 M NaOH was added. Then 3.0 g of Mg₃Al₁-LDHs was added into the Ru(OH)₆^{3−}-containing solution and the resulting suspension was maintained at 50 °C for 6 h under magnetic stirring (400 rpm). The resulting dark grey slurry was filtered. The solid was washed with deionized water and 95% ethanol until the filtrate was neutral, and dried under vacuum in an oven at 40 °C for 12 h.

RuCl₃/Mg₃Al₁-LDHs-I was prepared as follows: Typically, 65 mg of RuCl₃·xH₂O was dissolved in a certain volume of 95% ethanol, and then 3.0 g of Mg₃Al₁-LDHs was immersed. The resulting slurry was dried under vacuum in an oven at 60 °C for 12 h.

2.2.3. Reduction

The Ru loaded LDO samples were prepared by thermal treatment of Ru loaded LDHs under varied atmosphere. Ru/Mg₃Al₁-LDO-P-A was produced firstly by thermal treatment of Ru(OH)₆^{3−}/Mg₃Al₁-LDHs-P at 500 °C for 2 h under air atmosphere in a muffle furnace to produce RuO_x/Mg₃Al₁-LDO-P-A, and then the resulting RuO_x/Mg₃Al₁-LDO-P-A was thermally treated at 400 °C for 30 min under H₂ atmosphere in a tube furnace, with the temperature programmed from ambient to 500 or 400 °C in a heating rate of 5 °C/min. Ru/Mg₃Al₁-LDO-D-A, Ru/Mg₃Al₁-LDO-E-A, Ru/Mg₃Al₁-LDO-I-A, Ru/Mg₃Al_{0.9}Ga_{0.1}-LDO-P-A, or Ru/Mg₃Al_{0.9}Zr_{0.1}-LDO-P-A was produced by the thermal treatment of Ru(OH)₆^{3−}/Mg₃Al₁-LDHs-D, Ru(OH)_x/Mg₃Al₁-LDHs-E, RuCl₃/Mg₃Al₁-LDHs-I, Ru(OH)₆^{3−}/Mg₃Al_{0.9}Ga_{0.1}-LDHs-P, or Ru(OH)₆^{3−}/Mg₃Al_{0.9}Zr_{0.1}-LDHs-P in the same procedure. Ru/Mg₃Al₁-LDO-P-N was prepared by the thermal treatment of Ru(OH)₆^{3−}/Mg₃Al₁-LDHs-P in the same procedure as that for Ru/Mg₃Al₁-LDO-P-A, except that Ru(OH)₆^{3−}/Mg₃Al₁-LDHs-P was first thermally treated at 500 °C for 2 h under N₂ atmosphere in a tube furnace. For comparison, pristine Mg₃Al₁-LDO (without Ru loaded) was produced by thermal treatment of Mg₃Al₁-LDHs following the same procedures as that for Ru/Mg₃Al₁-LDO-P-A.

2.3. Characterizations

Powder X-ray diffraction (XRD) patterns were taken on a Shimadzu XRD-6000 diffractometer operated at 40 kV and 30 mA using a Cu K α radiation ($\lambda = 0.1541$ nm), with a scanning angle (2θ) range of $3\text{--}80^\circ$ at a scan speed of $10^\circ \text{ min}^{-1}$. Quantitative analysis for metal elements were performed on a Shimadzu ICPS-7500 inductively coupled plasma emission spectrometer (ICP-ES). Typically, 20 mg of solid sample was dissolved in aqua regia and heated at 120°C for 6 h in a Teflon autoclave. The resulting solution was then transferred to a 100 mL volumetric flask and diluted to volume with deionized water. H_2 -temperature programmed reduction (H_2 -TPR) measurements were carried out on a Micromeritics ChemiSorb 2750 chemisorption instrument with a thermal conductivity detector (TCD). In each case, 100 mg of sample was pre-treated in a flow of Ar (40 mL/min) at 150°C for 1 h and then cooled to room temperature. The H_2 -TPR profile was recorded from 50°C to 700°C at a temperature-programmed rate of 10°C/min in a flow of 10 vol% H_2 -Ar (40 mL/min). Scanning electron microscopic (SEM) images were taken on a Zeiss Supra 55 (Zeiss Ltd., Germany). Low-temperature N_2 adsorption/desorption experiments were carried out on Quantachrome Autosorb-1 C-VP analyzer. The samples were outgassed under vacuum at 100°C for 6 h prior to the measurement. The specific surface area was calculated by Brunauer-Emmett-Teller (BET) method. Aberration-corrected high-angle annular dark-field scanning transmission electron microscopic (Ac-HAADF-STEM) images and element energy dispersive spectroscopic (EDS) mappings were taken on a JEOL JEM-ARM200F electron microscope capable of sub-ångström resolution. The samples were dispersed onto a copper grid coated with a thin holey carbon film for the measurements. The X-ray absorption spectra (XAS) of Ru K-edge were measured at the beamline 1W1B station of Beijing Synchrotron Radiation Facility (BSRF). The storage rings of BSRF was operated at 2.5 GeV with an average current of 250 mA by top-up mode. Using Si (111) double-crystal monochromator, the data of Ru samples were recorded in transmission mode using ionization chamber. All spectra were collected in ambient conditions. The acquired X-ray absorption near-edge structure (XANES) spectra were processed according to the standard procedures using the ATHENA module implemented in the IFEFFIT software packages [38]. The k^3 -weighted extended X-ray absorption fine structure (EXAFS) spectra were obtained by subtracting the post-edge background from the overall absorption followed by normalizing with respect to the edge-jump step, and subsequently, the k^3 -weighted $\chi(k)$ data of Ru K-edge were Fourier transformed (FT) to real (R) space by use of a hanning windows ($\Delta k = 1.0 \text{ \AA}^{-1}$) to separate the EXAFS contributions from different coordination shells [38]. In order to obtain the quantitative structural parameters around central Ru atoms, least-squares curve parameter fitting were carried out by use of the ARTEMIS module implemented in the IFEFFIT software packages [38]. Wavelet transform (WT) of Ru K-edge EXAFS spectra were carried out by use of program HAMA developed by Funke and Chukalina [39,40]. Quasi in-situ surface elemental analysis were performed by use of a Shimadzu Kratos Axis Supra X-ray photoelectron spectroscopic (XPS) spectrometer equipped with a monochromated Al-K X-ray source (1486.6 eV) at a pass energy of 40 eV. Prior to measurement, the reduced Ru-containing samples were pre-treated at 400°C in a flow of 10 vol% H_2 -Ar atmosphere for 30 min (40 mL/min), and then flushed with Ar (40 mL/min) at 400°C for 30 min. The pre-treated sample was transferred to the analysis chamber of XPS spectrometer without exposure to air. C_{1s} peak at 284.8 eV was used as the calibration peak. ^{27}Al magic-angle spinning nuclear magnetic resonance (MAS NMR) analysis was carried out on a Bruker Avance Bruker AVANCE III 400WB with a commercial 4 mm MAS NMR probe. The aqueous solution of $\text{Al}(\text{NO}_3)_3$ in 1 mol/L was used as a reference, assigned a chemical shift of 0.0 ppm.

The CO_2 -temperature programmed desorption (CO_2 -TPD) and NH_3 -TPD were carried out on a Micromeritics AutoChem II 2920 chemisorption instrument with a thermal conductivity detector (TCD).

Typically, 100 mg of sample was pretreated in a flow of Ar (40 mL/min) at 200°C for 1 h followed by cooling to 80°C , afterward, CO_2 was fed into the system until saturation, and then weakly physically adsorbed CO_2 was removed by a flow of Ar. The CO_2 -TPD profiles were recorded from 30°C to 700°C at a heating rate of 10°C/min in a flow of Ar (40 mL/min). For the NH_3 -TPD measurement, a similar procedure was followed, except for the introduction of NH_3 into the system at 100°C . In-situ Fourier transform infrared (FT-IR) spectra were recorded on a Nicolet iS50FT-IR spectrometer equipped with BaF $_2$ windows and a mercury-cadmium-telluride (MCT) detector cooled by liquid nitrogen, with a resolution of 4 cm^{-1} and an accumulation of 32 scans in the range of $800\text{--}4000 \text{ cm}^{-1}$. For in-situ CO adsorption-desorption, the sample was pressed into a self-supporting wafer, loaded into an in-situ IR cell, and then pretreated in a flow of 10 vol% H_2 -Ar (40 mL/min) at 400°C for 30 min, followed by purging with Ar (40 mL/min) for 30 min at 400°C and cooling in Ar to 50°C . After the background spectrum was recorded, CO was introduced until adsorption equilibrium was reached. Subsequently, the evacuation of adsorbed CO was carried out for 30 min and the FT-IR spectra were recorded consecutively at intervals during the evacuation process. For in-situ ethanol adsorption-desorption, the sample was pressed into a self-supporting wafer, loaded into an in-situ IR cell, and then pretreated in a flow of 10 vol% H_2 -Ar (40 mL/min) at 400°C for 30 min, followed by purging with Ar (40 mL/min) for 30 min at 400°C and cooling in Ar to 50°C . In the cooling procedure, the background spectra were recorded at 400°C , 350°C , 300°C , 250°C , 200°C , 150°C , 100°C , and 50°C , respectively. Ethanol was bubbled into the IR cell by Ar flow (5 mL/min) at 50°C until the equilibrium was reached, and subsequently, the adsorbed ethanol was purged under Ar flow (5 mL/min) until the spectra showed no change and the spectrum for ethanol adsorption was recorded. The temperature was increased under Ar with a heating rate of 10°C/min and maintained at 100°C for 10 min, and the spectrum at 100°C was recorded. The FT-IR spectrum at 100°C , 150°C , 200°C , 250°C , 300°C , 350°C and 400°C was recorded in a similar way. For in-situ FT-IR study of acetaldehyde adsorption, after the sample was pre-treated in the same procedure as for the ethanol adsorption, the background spectrum was recorded at 10°C under vacuum. Then acetaldehyde vapor was introduced into the in-situ IR cell until equilibrium was reached, and subsequently, the adsorbed acetaldehyde was purged under Ar flow until the spectra showed no change and the spectrum for acetaldehyde adsorption was recorded. The FT-IR spectra of adsorbed pyridine were taken for surface acidity measurements, after the pretreatment of sample in the in-situ IR cell, the background spectrum was recorded at 50°C under vacuum. Then pyridine vapor was introduced until equilibrium was reached. The adsorbed pyridine was desorbed at 150°C under Ar flow (5 mL/min) until the spectrum showed no change and the final spectrum was recorded.

2.4. Catalytic tests

The ethanol coupling reaction was performed in a fixed-bed reactor with a stainless steel tubular reactor (10 mm external diameter, 38 cm length) equipped with on-line gas chromatography (Shimadzu GC 2014C). Typically, 500 mg of catalyst (20–40 mesh) was loaded into the reactor tube and the remaining volume of the reactor tube was filled with quartz sand (20–40 mesh). Prior to reaction, the catalyst was pre-treated in situ in a flow of 10 vol% H_2 -Ar (40 mL/min) at 400°C for 30 min. Then the reactor was controlled to the reaction temperature of 350°C and the carrier gas was changed to N_2 flow (40 mL/min). The chromatographically pure ethanol (99.8%) was pumped into the vaporizing chamber using a high-performance liquid chromatography pump at $33 \mu\text{L/min}$ (molar concentration of ethanol = 25%, WHSV = 3.2 h^{-1}), and then the vapor was introduced into the reaction tube by carrier gas. During the reaction, the products were identified by GC-MS (Agilent 7200 Q-TOF GC/MS) and analyzed quantitatively on an on-line gas chromatography (Shimadzu GC 2014 C) equipped with a GSBP-INOWAX column (30 m, 0.25 mm inner diameter). The ethanol

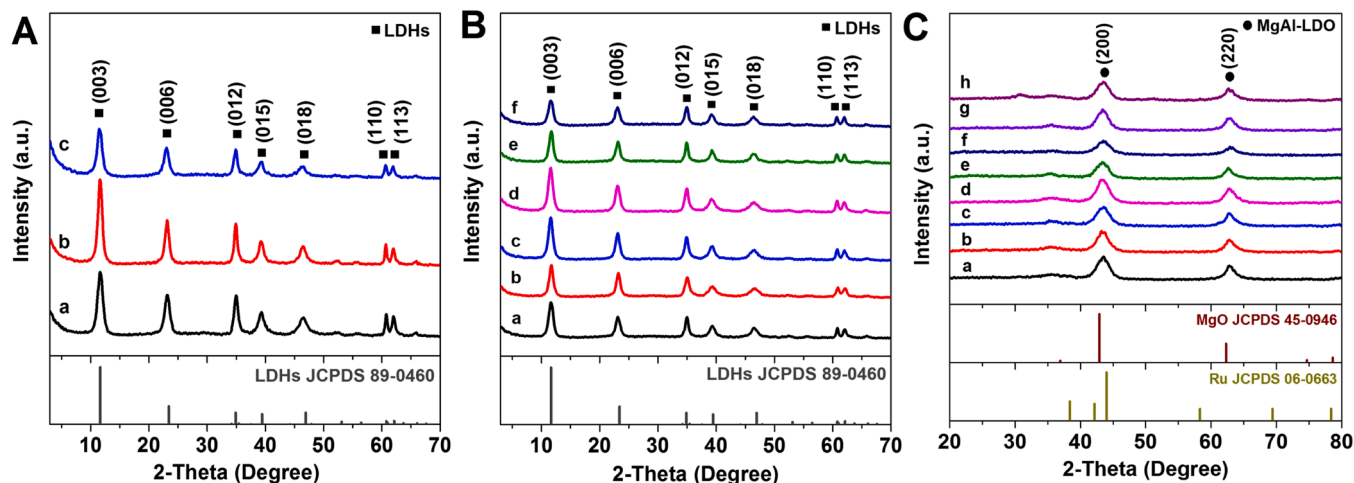


Fig. 1. (A) XRD patterns of (a) $\text{Mg}_3\text{Al}_1\text{-CO}_3^{2-}\text{-LDHs}$, (b) $\text{Mg}_3\text{Al}_{0.9}\text{Ga}_{0.1}\text{-CO}_3^{2-}\text{-LDHs}$, and (c) $\text{Mg}_3\text{Al}_{0.9}\text{Zr}_{0.1}\text{-CO}_3^{2-}\text{-LDHs}$. (B) XRD patterns of (a) $[\text{Ru}(\text{OH})_6]^{3-}/\text{Mg}_3\text{Al}_1\text{-CO}_3^{2-}\text{-LDHs-P}$, (b) $[\text{Ru}(\text{OH})_6]^{3-}/\text{Mg}_3\text{Al}_1\text{-CO}_3^{2-}\text{-LDHs-D}$, (c) $\text{Ru}(\text{OH})_x/\text{Mg}_3\text{Al}_1\text{-CO}_3^{2-}\text{-LDHs-E}$, (d) $\text{RuCl}_3/\text{Mg}_3\text{Al}_1\text{-CO}_3^{2-}\text{-LDHs-I}$, (e) $[\text{Ru}(\text{OH})_6]^{3-}/\text{Mg}_3\text{Al}_{0.9}\text{Ga}_{0.1}\text{-CO}_3^{2-}\text{-LDHs-P}$ and (f) $[\text{Ru}(\text{OH})_6]^{3-}/\text{Mg}_3\text{Al}_{0.9}\text{Zr}_{0.1}\text{-CO}_3^{2-}\text{-LDHs-P}$. (C) XRD patterns of (a) $\text{Mg}_3\text{Al}_1\text{-LDO}$, (b) 1.04 wt% $\text{Ru}/\text{Mg}_3\text{Al}_1\text{-LDO-P-A}$, (c) 1.02 wt% $\text{Ru}/\text{Mg}_3\text{Al}_1\text{-LDO-D-A}$, (d) 0.95 wt% $\text{Ru}/\text{Mg}_3\text{Al}_1\text{-LDO-E-A}$, (e) 0.97 wt% $\text{Ru}/\text{Mg}_3\text{Al}_1\text{-LDO-I-A}$, (f) 1.08 wt% $\text{Ru}/\text{Mg}_3\text{Al}_1\text{-LDO-P-N}$, (g) 1.11 wt% $\text{Ru}/\text{Mg}_3\text{Al}_{0.9}\text{Ga}_{0.1}\text{-LDO-P-A}$, and (h) 1.07 wt% $\text{Ru}/\text{Mg}_3\text{Al}_{0.9}\text{Zr}_{0.1}\text{-LDO-P-A}$.

conversion, product selectivity, carbon balance were calculated as follows:

$$\text{Ethanol conversion}(\%) = \frac{F_{in} - F_{unreacted}}{F_{in}} \times 100\% \quad (1)$$

$$\text{Selectivity}(\%) = \frac{x \text{ mol of carbon in the target product}}{x \text{ mol of carbon in all products}} \times 100\% \quad (2)$$

$$\text{Carbon balance}(\%) = \frac{x \text{ mol of carbon in all products}}{x \text{ mol of carbon in ethanol reacted}} \times 100\% \quad (3)$$

where F_{in} and $F_{unreacted}$ are the moles of input ethanol and unreacted ethanol.

The acetaldehyde condensation was also performed in the fixed-bed reactor with a stainless-steel tubular reactor (10 mm external diameter, 38 cm length) equipped with on-line gas chromatography (Shimadzu GC 2010). The procedures are the same as the ethanol coupling reaction

except that the 40 $\mu\text{L}/\text{min}$ of mixture of acetaldehyde/hexane (acetaldehyde in 10 wt%) was introduced to the system. During the reaction, the products were analyzed quantitatively on an on-line gas chromatography (Shimadzu GC 2014 C) equipped with a HP-624Si column (30 m, 0.25 mm inner diameter). The acetaldehyde conversion and product selectivity were calculated as follows:

$$\text{Acetaldehyde conversion}(\%) = \frac{F_{in} - F_{unreacted}}{F_{in}} \times 100\% \quad (4)$$

$$\text{Selectivity}(\%) = \frac{x \text{ mol of carbon in the target product}}{x \text{ mol of carbon in all products}} \times 100\% \quad (5)$$

where F_{in} and $F_{unreacted}$ are the moles of input and unreacted acetaldehyde.

Calculations of mass transfer limitations on 1.04 wt% $\text{Ru}/\text{Mg}_3\text{Al}_1\text{-LDO-P-A}$ at 623 K, 0.1 MPa with ethanol conversion of 30% were carried

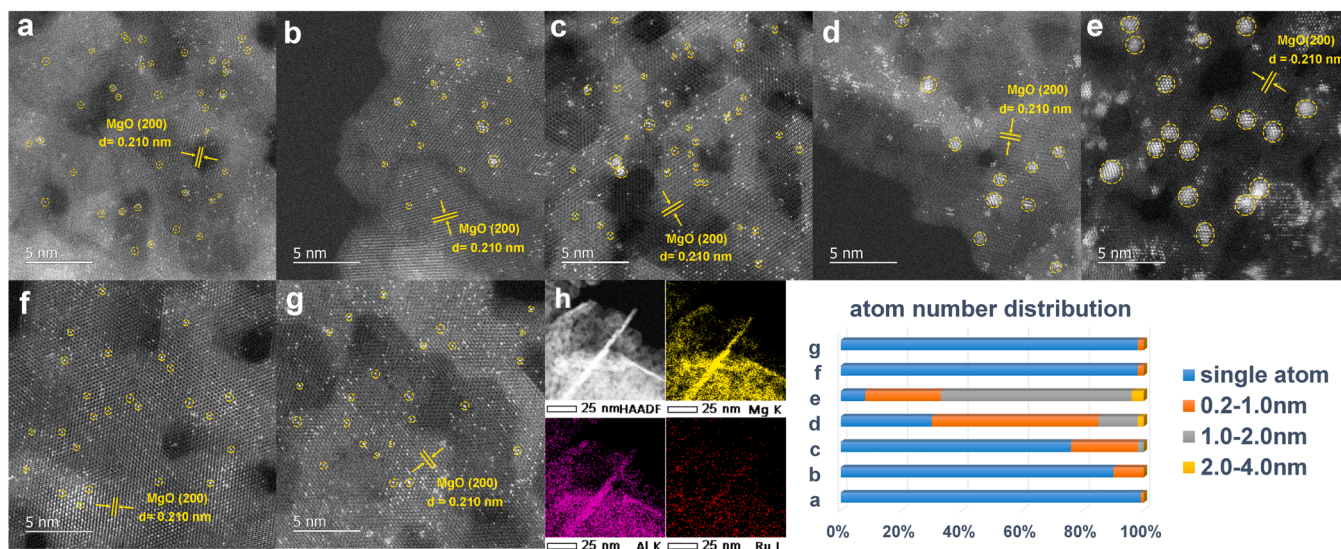


Fig. 2. Ac-HAADF-STEM images and the corresponding atom number distribution of (a) 1.04 wt% $\text{Ru}/\text{Mg}_3\text{Al}_1\text{-LDO-P-A}$, (b) 1.02 wt% $\text{Ru}/\text{Mg}_3\text{Al}_1\text{-LDO-D-A}$, (c) 0.95 wt% $\text{Ru}/\text{Mg}_3\text{Al}_1\text{-LDO-E-A}$, (d) 0.97 wt% $\text{Ru}/\text{Mg}_3\text{Al}_1\text{-LDO-I-A}$, (e) 1.08 wt% $\text{Ru}/\text{Mg}_3\text{Al}_1\text{-LDO-P-N}$, (f) 1.11 wt% $\text{Ru}/\text{Mg}_3\text{Al}_{0.9}\text{Ga}_{0.1}\text{-LDO-P-A}$, (g) 1.07 wt% $\text{Ru}/\text{Mg}_3\text{Al}_{0.9}\text{Zr}_{0.1}\text{-LDO-P-A}$, and (h) EDS elemental mapping for 1.04 wt% $\text{Ru}/\text{Mg}_3\text{Al}_1\text{-LDO-P-A}$. For each sample, more than 500 Ru atoms were counted from varied regions of Ac-HAADF-STEM images.

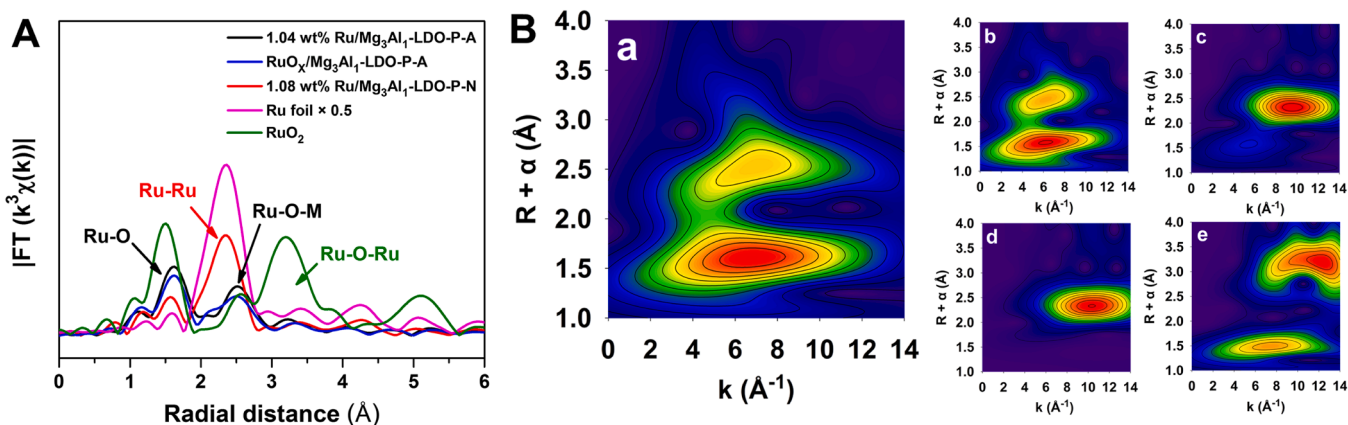


Fig. 3. (A) Fourier transforms of k^3 -weighted Ru EXAFS spectra and (B) Wavelet transform of the EXAFS spectra for (a) 1.04 wt% Ru/Mg₃Al₁-LDO-P-A, (b) RuO_x/Mg₃Al₁-LDO-P-A, (c) 1.08 wt% Ru/Mg₃Al₁-LDO-P-N, (d) Ru foil, and (e) RuO₂.

out using the Mears and Weisz-Prater analyses (see Supporting Information for detailed calculation) [41,42]. Mears Criterion for external diffusion and Weisz-Prater Criterion for internal diffusion were $0.02 < 0.15$ and $0.08 < 1$, respectively, suggesting the absence of diffusion limitation in this work.

3. Results and discussion

3.1. Ru dispersion

Fig. 1 shows the XRD patterns of as-prepared layered double hydroxides (LDHs), Ru (III)-loaded layered double hydroxides, and Ru-loaded layered double oxides (LDO). The (003), (006), (012), (015), (018), (110), and (113) reflections at about 11.7° , 23.0° , 35.0° , 39.5° , 46.5° , 60.7° and 62.0° , characteristic of hydrotalcite structure are clearly observed for the LDHs with varied layer composition (Fig. 1A) and with Ru loaded by varied procedure (Fig. 1B). No reflections of other phases are observed in each case. The loading of Ru precursors causes no obvious change of XRD patterns. The temperature for complete reduction of RuO_x species in RuO_x-loaded LDO was detected by H₂-TPR (Fig. S1) as being around 400°C in each case. After thermal treatment under first air or N₂ and then H₂ atmosphere, the resulting Ru-loaded LDO exhibits (200) and (220) reflections typical of MgAl-LDO in each case (Fig. 1C). No obvious reflections of metallic Ru and spinel phases are observed. The Ru loading was determined by ICP technique in the range from 0.9 wt% to 1.2 wt%. The molar ratio of Mg to Al was determined by ICP technique as being about 3.0.

The dispersion of Ru can be resolved from Ac-HAADF-STEM images (Fig. 2). By varying Ru (III)-loaded method and thermal treatment procedure, Ru dispersion has been tailored as $> 99\%$ atomic Ru (Fig. 2a), 90% atomic Ru coexisting with 10% 0.2–1.0 nm clusters (Fig. 2b), 76% atomic Ru coexisting with 22% 0.2–1.0 nm nanoclusters and 2% > 1.0 nm nanoparticles (Fig. 2c), 30% atomic Ru coexisting with 55% 0.2–1.0 nm nanoclusters and 15% > 1.0 nm nanoparticles (Fig. 2d), and 67% > 1.0 nm nanoparticles coexisting with 8% atomic Ru and 25% 0.2–1.0 nm nanoclusters (Fig. 2e). The pristine Mg₃Al₁-LDO and Ru-loaded Mg₃Al₁-LDO show similar morphology, BET surface area, and pore size distribution (Fig. S2 and Fig. S3). On Ga- or Zr- introduced LDO (Mg₃Al_{0.9}Ga_{0.1}-LDO or Mg₃Al_{0.9}Zr_{0.1}-LDO), Ru dispersion (Fig. 2f and g) is similar to that on Mg₃Al₁-LDO (Fig. 2a), with similar Ru-loading and thermal treatment procedure, in 98% atomic Ru. EDS (Fig. 2h) mappings of 1.04 wt% Ru/Mg₃Al₁-LDO-P-A display that atomic Ru is uniformly distributed on Mg₃Al₁-LDO.

In the Fourier transforms of k^3 -weighted Ru EXAFS spectra (Fig. 3A), no Ru-Ru interactions were identified in either 1.04 wt% Ru/Mg₃Al₁-LDO-P-A or RuO_x/Mg₃Al₁-LDO-P-A, while obvious Ru-Ru interactions were identified in the 1.08 wt% Ru/Mg₃Al₁-LDO-P-N, indicating the

Table 1
EXAFS fitting parameters at the Ru K-edge for various samples.

Samples	Shell	R (Å) ^a	N ^b	σ^2 (Å ² ·10 ⁻³) ^c	ΔE_0 (eV) ^d	R factor (%)
1.04 wt% Ru/Mg ₃ Al ₁ -LDO-P-A	Ru-O	2.08	4.3	4.4	6.4	1.1
	Ru-O-M	2.98	4.3	5.3	-1.4	
RuO _x /Mg ₃ Al ₁ -LDO-P-A	Ru-O	2.08	4.2	6.8	4.1	0.8
	Ru-O-M	2.97	4.2	8.4	-2.9	
1.08 wt% Ru/Mg ₃ Al ₁ -LDO-P-N	Ru-O	1.98	2.7	9.0	-3.1	1.0
	Ru-	2.68	5.0	6.3	6.2	
	Ru					
Ru foil	Ru-	2.68	12	3.0	-4.5	0.8
	Ru					
RuO ₂	Ru-O	1.98	6	3.2	-4.4	1.0

^a R: bond distance.

^b N: coordination number.

^c σ^2 : Debye-Waller factor.

^d ΔE_0 : the inner potential correction. R factor: goodness of fit. S_0^2 was set as 0.95/0.90 for Ru-O/Ru-Ru, which were obtained from the experimental EXAFS fit of reference RuO₂ and Ru foil by fixing coordination number as the known crystallographic value and was fixed to all the samples. Ru foil parameter is from data 41515-ICSD. RuO₂ parameter is from data 66939-ICSD. Error bounds (accuracies) of the above structural parameters obtained by EXAFS spectra were estimated as N, $\pm 20\%$; R, $\pm 1\%$; σ^2 , $\pm 20\%$; ΔE_0 , $\pm 20\%$.

isolate Ru species in 1.04 wt% Ru/Mg₃Al₁-LDO-P-A and RuO_x/Mg₃Al₁-LDO-P-A while Ru particles in 1.08 wt% Ru/Mg₃Al₁-LDO-P-N. The EXAFS identifications of 1.04 wt% Ru/Mg₃Al₁-LDO-P-A and 1.08 wt% Ru/Mg₃Al₁-LDO-P-N are in agreement with the structural determinations by Ac-HAADF-STEM (Fig. 2), and also supported by the FT-IR spectra of CO adsorption-desorption (Fig. S4). In the FT-IR spectra of CO adsorption-desorption on Ru-loaded LDO, two adsorption bands at $2035\text{--}2050\text{ cm}^{-1}$ and $1960\text{--}1976\text{ cm}^{-1}$, assigned to the linear CO adsorption on atomic Ru [43,44], are clearly observed on 1.04 wt% Ru/Mg₃Al₁-LDO-P-A, suggesting the atomically dispersed Ru in 1.04 wt% Ru/Mg₃Al₁-LDO-P-A. Besides the band at $1960\text{--}1976\text{ cm}^{-1}$, a new band at 2012 cm^{-1} , assigned to the linear CO adsorption on Ru nanoparticles [44], is observed on 1.08 wt% Ru/Mg₃Al₁-LDO-P-N, indicative of the presence of Ru nanoparticles in Ru/Mg₃Al₁-LDO-P-N. Similar results are detected on 1.11 wt% Ru/Mg₃Al_{0.9}Ga_{0.1}-LDO-P-A and 1.07 wt% Ru/Mg₃Al_{0.9}Zr_{0.1}-LDO-P-A to that on 1.04 wt% Ru/Mg₃Al₁-LDO-P-A, indicative of the atomically dispersed Ru in 1.11 wt% Ru/Mg₃Al_{0.9}Ga_{0.1}-LDO-P-A and 1.07 wt% Ru/Mg₃Al_{0.9}Zr_{0.1}-LDO-P-A. These results are well consistent with the Ac-HAADF-STEM, EXAFS, and Wavelet transform of EXAFS spectra results. In the wavelet transforms of the EXAFS spectra (Fig. 3B), the WT contour plots of 1.04 wt%

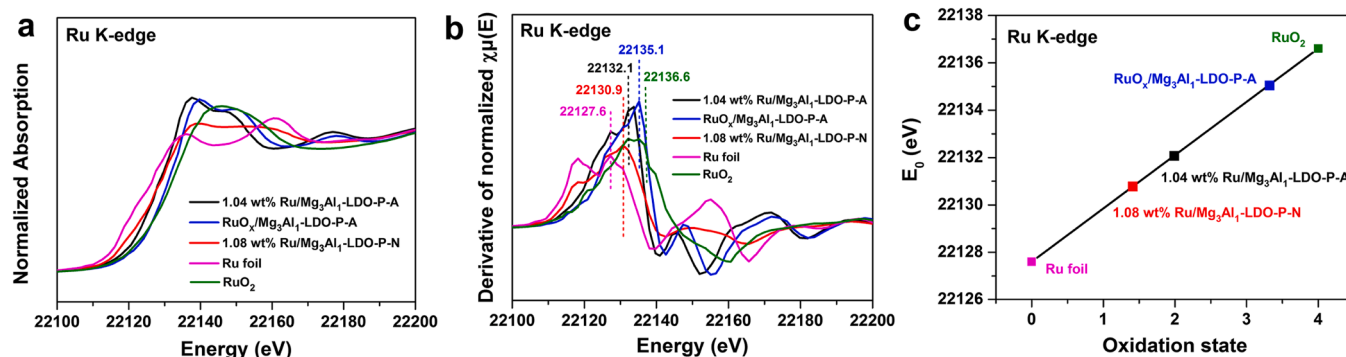


Fig. 4. (a) Ru K-edge XANES spectra, (b) first-derivative XANES curves, and (c) oxidation state analysis for Ru K-edge.

Ru/Mg₃Al₁-LDO-P-A and RuO_x/Mg₃Al₁-LDO-P-A show two intensities, corresponding to Ru-O and Ru-O-M coordination. No intensity maximum related to Ru-Ru contribution can be resolved at high coordination shells, which has been observed in the WT plot of 1.08 wt% Ru/Mg₃Al₁-LDO-P-N and Ru foil. The WT contour plots of 1.04 wt% Ru/Mg₃Al₁-LDO-P-A and RuO_x/Mg₃Al₁-LDO-P-A are also different from RuO₂. The results indicate that the Ru species in 1.04 wt% Ru/Mg₃Al₁-LDO-P-A and RuO_x/Mg₃Al₁-LDO-P-A are dispersed in atomic scale. From the spectra of RuO_x/Mg₃Al₁-LDO-P-A, it can be deduced that atomic Ru has been formed by the calcination of [Ru(OH)₆]³⁺/Mg₃Al₁-CO₃²⁻-LDHs-P under air atmosphere.

To explore further the coordination structure of atomic Ru, the Ru K-edge EXAFS fitting have been performed. The parameters based on the EXAFS are shown in Table 1. The detailed fitting results are presented in Fig. S5 for k space and Fig. S6 for R space. Model-based EXAFS fitting further indicates that the Ru atoms in 1.04 wt% Ru/Mg₃Al₁-LDO-P-A possesses a Ru-O coordination of 4.3 without Ru-Ru coordination. The EXAFS fitting parameter R (Å) is defined as the distance between absorber and backscatter atoms, also called bond distance, indicates that

the mean bond length of Ru-O is 2.08 Å, and meanwhile, the Mg or Al atom in the support forms a Ru-O-M (M stands for Mg or Al atom) bond with Ru atom through the oxygen bridge [45], with a distance between Ru atom and M of 2.98 Å. In the ²⁷Al MAS NMR results (Fig. S7, a), the loading of atomic Ru increases the signal intensity of four-coordinated [46] Al species, consistent with the formation of Ru-O-M bond.

The electronic structure of atomic Ru has been investigated by XANES (Fig. 4) and XPS (Fig. S8) spectra. The absorption edge of 1.04 wt% Ru/Mg₃Al₁-LDO-P-A (atomic Ru dominant) and 1.08 wt% Ru/Mg₃Al₁-LDO-P-N (Ru cluster and 1.0–2.0 nm particle dominant) are very close, located between the absorption edge of Ru foil and RuO₂, while the absorption edge of RuO_x/Mg₃Al₁-LDO-P-A approaches that of RuO₂ (Fig. 4a). From the first-derivative of absorption edge in Fig. 4a, the absorption threshold (E₀) was obtained (Fig. 4b). Then the E₀ value was plotted as a function of oxidation state (Fig. 4c). The linear fitting result in Fig. 4c clearly indicates that either the atomic Ru in 1.04 wt% Ru/Mg₃Al₁-LDO-P-A or the Ru cluster and 1.0–2.0 nm particle in 1.08 wt% Ru/Mg₃Al₁-LDO-P-N deviate from both Ru⁰ but is not Ru⁴⁺ in RuO₂. In the XPS spectra (Fig. S8), 1.04 wt% Ru/Mg₃Al₁-LDO-P-A shows

Table 2

Catalytic results of catalysts for ethanol coupling to C₄₊ alcohols.

Entry	Catalysts	The proportion of atomic Ru/%	EtOH Conv./%	Selectivity/%							Carbon balance/%
				diethyl ether	acetaldehyde	n-butanol	n-butanol	2-ethyl-1-butanol	n-hexanol	C ₄₊ alcohols	
1	Mg ₃ Al ₁ -LDO	–	13.2	25.8	6.5	3.6	54.5	0.6	3.9	59.0	95
2	1.04 wt% Ru/Mg ₃ Al ₁ -LDO-P-A	99	29.6 (30.0)	7.2(7.0)	6.0(6.1)	0.8 (1.3)	70.1 (70.8)	2.8(2.2)	9.7(9.0)	82.6(82.0)	94(92)
3	Mg ₃ Al ₁ -LDO ^a	–	2.1	33.2	3.4	0.7	55.8	–	2.3	58.1	96
4	1.04 wt% Ru/Mg ₃ Al ₁ -LDO-P-A ^a	99	6.3	6.6	6.0	1.0	73.2	4.4	5.6	83.2	95
5	1.02 wt% Ru/Mg ₃ Al ₁ -LDO-D-A	90	28.3 (27.6)	9.2(8.6)	8.3(8.7)	2.2 (2.0)	66.2 (67.0)	2.2(1.7)	8.2(7.3)	76.6(76.0)	93(92)
6	0.95 wt% Ru/Mg ₃ Al ₁ -LDO-E-A	76	25.9	9.7	10.5	4.1	61.7	1.8	7.5	71.0	93
7	0.97 wt% Ru/Mg ₃ Al ₁ -LDO-I-A	30	25.0	3.7	21.4	6.8	52.7	3.3	4.9	60.9	80*
8	1.08 wt% Ru/Mg ₃ Al ₁ -LDO-P-N	8	20.2	3.5	27.5	6.9	45.7	3.1	3.4	52.2	72*
9	RuO _x /Mg ₃ Al ₁ -LDO-P-A ^b	–	16.0	17.4	8.3	2.7	63.9	0.3	1.2	65.4	94
10	1.11 wt% Ru/Mg ₃ Al _{0.9} Ga _{0.1} -LDO-P-A	98	27.5	12.0	8.3	4.2	63.6	2.0	4.7	70.3	91
11	1.07 wt% Ru/Mg ₃ Al _{0.9} Zr _{0.1} -LDO-P-A	98	22.8	26.1	7.3	3.8	53.4	1.0	2.5	56.9	92

If not specially indicated, conversion and selectivity were obtained at steady-state; reaction conditions: 500 mg catalyst, T = 350 °C, P_(N₂) = 0.1 MPa, flowing rate = 40 mL·min⁻¹, WHSV = 3.2 h⁻¹. ^aConversion and selectivity were obtained at steady-state; reaction conditions: 500 mg catalyst, T = 300 °C, P_(N₂) = 0.1 MPa, flowing rate = 40 mL·min⁻¹, WHSV = 3.2 h⁻¹. ^bConversion and selectivity were obtained at initial-state; reaction conditions: 500 mg catalyst, T = 350 °C, P_(N₂) = 0.1 MPa, flowing rate = 40 mL·min⁻¹, WHSV = 3.2 h⁻¹. Other products include ethylene, ethyl acetate, hexanal, 2-ethyl-butanol, etc. *The lower carbon balance was caused by the decarbonylation of acetaldehyde. The data in the parenthesis are reproduced ones.

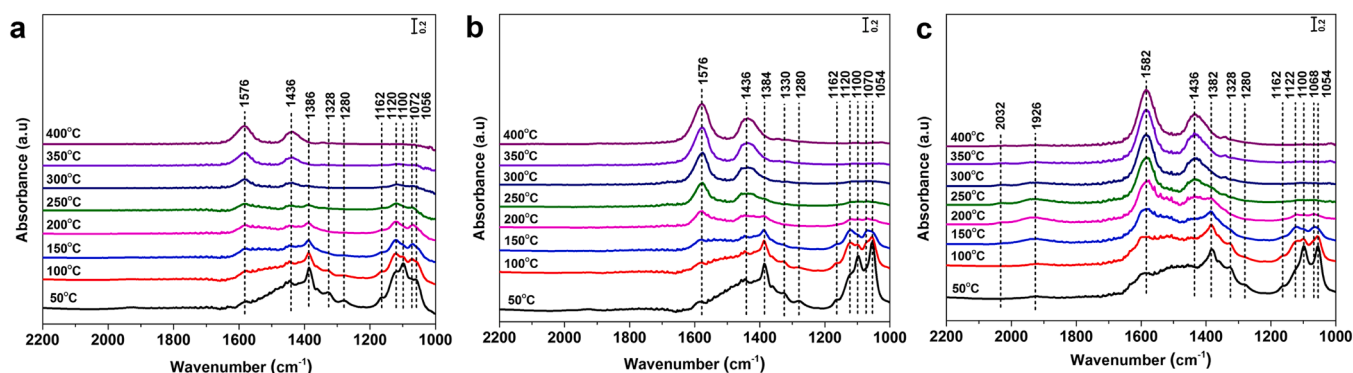


Fig. 5. In-situ FT-IR spectra of ethanol adsorption at 50 °C followed by desorption at 50 °C, 100 °C, 150 °C, 200 °C, 250 °C, 300 °C, 350 °C, and 400 °C on (a) $\text{Mg}_3\text{Al}_1\text{-LDO}$, (b) 1.04 wt% $\text{Ru}/\text{Mg}_3\text{Al}_1\text{-LDO-P-A}$, and (c) 1.08 wt% $\text{Ru}/\text{Mg}_3\text{Al}_1\text{-LDO-P-N}$.

a dominant binding energy of Ru 3d at 282.0 eV, which can be as assigned to Ru^{2+} (Fig. S8, b). 1.08 wt% $\text{Ru}/\text{Mg}_3\text{Al}_1\text{-LDO-P-N}$ shows one binding energy of Ru 3d at 282.0 eV and the other at 280.0 eV, which can be attributed to $[\text{47,48}] \text{Ru}^{2+}$ and Ru^0 (Fig. S8, c). The deviation from Ru^0 is proposed to result from the strong interaction between atomic Ru and $\text{Mg}_3\text{Al}_1\text{-LDO}$ in 1.04 wt% $\text{Ru}/\text{Mg}_3\text{Al}_1\text{-LDO-P-A}$, which is supported by H_2 -TPR results (Fig. S1). In the H_2 -TPR profiles, the Ru species in 1.04 wt% $\text{Ru}/\text{Mg}_3\text{Al}_1\text{-LDO-P-A}$ can be completely reduced under the conditions performed at this work. The strong interactions between atomic Ru and $\text{Mg}_3\text{Al}_1\text{-LDO}$ result in an apparent oxidized state of Ru sites.

3.2. Ru dispersion and ethanol coupling

The Ru dispersion and catalytic ethanol coupling results are shown in Table 2 and time-on-stream analysis are shown in Fig. S9. Comparing $\text{Mg}_3\text{Al}_1\text{-LDO}$ with 1.04 wt% $\text{Ru}/\text{Mg}_3\text{Al}_1\text{-LDO-P-A}$, the atomic Ru supported on $\text{Mg}_3\text{Al}_1\text{-LDO}$ obviously improves ethanol reaction activity and C_{4+} alcohols selectivity, with ethanol conversion increases from 13.2% to 29.6% and C_{4+} alcohols selectivity increases from 59.0% to 82.6% (Table 2, entries 1 and 2), a selectivity of 82.6% to C_{4+} alcohols under an ethanol conversion of 29.6%, which is higher than the results at an ethanol conversion of > 25% reported till now. Since the startup for ethanol coupling to C_{4+} alcohols needs ethanol dehydrogenation to intermediate acetaldehyde, accompanied by competitive ethanol dehydration to diethyl ether, the introduction of atomic Ru promotes ethanol dehydrogenation, suppressing the production of diethyl ether as side-product from a selectivity of 25.8–7.2%. In addition, the introduction of atomic Ru enhances acetaldehyde condensation and hydrogen transfer (e.g. n-butanal to n-butanol), thus improving C_{4+} alcohols selectivity. In order to further illustrate the role of atomic Ru in promoting ethanol dehydrogenation, acetaldehyde condensation and hydrogenation of n-butanal by hydrogen transfer, the reaction temperature decreases from 350 to 300 °C (Table 2, entries 3 and 4). It can be seen that under a lower temperature, the promotion effects of atomic Ru are more visible. The ethanol conversion increases from 2.1 on $\text{Mg}_3\text{Al}_1\text{-LDO}$ to 6.3% on atomic Ru supported $\text{Mg}_3\text{Al}_1\text{-LDO}$, and the C_{4+} alcohols selectivity increases from 58.1% to 83.2% with the production of ethyl ether suppressed from a selectivity of 33.2–6.6% (Table 2, entries 3 and 4). The $\text{Mg}_3\text{Al}_1\text{-LDO}$ (Fig. S9, a) and $\text{Mg}_3\text{Al}_1\text{-LDO}$ supported atomic Ru (Fig. S9, b–e) show excellent stability during the 700 min of time-on-stream reaction. In the Ac-HAADF-STEM of used 1.04 wt% $\text{Ru}/\text{Mg}_3\text{Al}_1\text{-LDO-P-A}$ (Fig. S10), atomic Ru are still clearly detected while no agglomeration of Ru particles is observed, showing excellent stability of the atomic Ru in ethanol coupling. As mentioned above, the atomic Ru forms strong interaction with oxygen sites on MgAl-LDO support surface, contributing to the excellent stability of supported atomic Ru. To further identify the active site for ethanol coupling to C_{4+} alcohols, the catalytic reaction has been performed with $\text{Ru}/\text{Mg}_3\text{Al}_1\text{-LDO}$ in reduced

proportion of atomic Ru (Table 2, entries 5–8). With reducing proportion of atomic Ru (Table 2, entries 2 and 5–8), both ethanol reaction and n-butanol selectivity gradually decreases. So the proportion of atomic Ru was further correlated (Fig. S11) with ethanol conversion and product selectivity. The ethanol conversion (Fig. S11, a) and the C_{4+} alcohols selectivity both increases with incremental atomic Ru, and the n-butanol selectivity decreases with incremental atomic Ru (Fig. S11, b). The results mean that atomic Ru is the active site more effective than Ru cluster or nanoparticle. To further investigate the role of atomic Ru in the contribution of acetaldehyde condensation, the reaction of acetaldehyde on 1.04 wt% $\text{Ru}/\text{Mg}_3\text{Al}_1\text{-LDO-P-A}$ and 1.08 wt% $\text{Ru}/\text{Mg}_3\text{Al}_1\text{-LDO-P-N}$ were performed, respectively. 96% of acetaldehyde conversion with nearly 99% selectivity of total acetaldehyde condensation products is obtained on atomic Ru supported $\text{Mg}_3\text{Al}_1\text{-LDO}$ while only 82% of acetaldehyde conversion on 1.08 wt% $\text{Ru}/\text{Mg}_3\text{Al}_1\text{-LDO-P-N}$ (Fig. S11, c), indicative the promotion of atomic Ru in acetaldehyde condensation. Interestingly, with Ru nanoparticles emerging, carbon balance visibly reduces from above 90–80% or 72% (Table 2, entries 7 and 8). Correspondingly, CH_4 and CO are detected in the gaseous products (Fig. S12), indicative of the decarbonylation of acetaldehyde. The catalytic coupling of ethanol has also been performed on $\text{RuO}_x/\text{Mg}_3\text{Al}_1\text{-LDO-P-A}$, the precursor for 1.04 wt% $\text{Ru}/\text{Mg}_3\text{Al}_1\text{-LDO-P-A}$. The conversion at initial-state (Table 2, entry 9) is similar to that on $\text{Mg}_3\text{Al}_1\text{-LDO}$, while much lower than on 1.04 wt% $\text{Ru}/\text{Mg}_3\text{Al}_1\text{-LDO-P-A}$. With the time-on-stream (Fig. S9, g), the ethanol conversion increases significantly and reached the level on 1.04 wt% $\text{Ru}/\text{Mg}_3\text{Al}_1\text{-LDO-P-A}$ in 100 min. The results indicate that the reduced Ru centers are the active sites for C-C coupling of ethanol since ethanol can reduce Ru oxide at high temperature.

3.3. The role of atomic Ru in ethanol coupling

To investigate the role of atomic Ru in ethanol coupling to C_{4+} alcohols, in-situ FT-IR spectra of ethanol adsorption/desorption and acetaldehyde adsorption on Ru sites have been recorded. As shown in Fig. 5, the ethanol adsorption on pristine support ($\text{Mg}_3\text{Al}_1\text{-LDO}$), atomic Ru (1.04 wt% $\text{Ru}/\text{Mg}_3\text{Al}_1\text{-LDO-P-A}$), and Ru nanoparticles (1.08 wt% $\text{Ru}/\text{Mg}_3\text{Al}_1\text{-LDO-P-N}$) at 50 °C all shows absorption bands around 1576, 1436, 1384, 1328, 1280, 1162, 1120, 1100, 1070 and 1054 cm^{-1} . According to previous reports [49,50], at 50 °C, the bands around 1436 and 1384 cm^{-1} can be assigned to the scissoring vibrations of CH_2 and CH_3 group ($\text{CH}_3 \delta$) in adsorbed ethoxide, the bands at 1280 cm^{-1} and 1162 cm^{-1} can be assigned to the stretching vibrations of C-O group (C-O ν) and C-C group (C-C ν) in η^2 -adsorbed acetaldehyde, the bands around 1120 and 1100 cm^{-1} can be assigned to the stretching vibrations of C-O group (C-O ν) in monodentate-adsorbed ethoxide, and the bands around 1070 and 1054 cm^{-1} can be assigned to the stretching vibrations of C-O group (C-O ν) in bidentate-adsorbed ethoxide. On $\text{Mg}_3\text{Al}_1\text{-LDO}$ (Fig. 5a), the monodentate adsorption of ethoxide at 1100 cm^{-1}

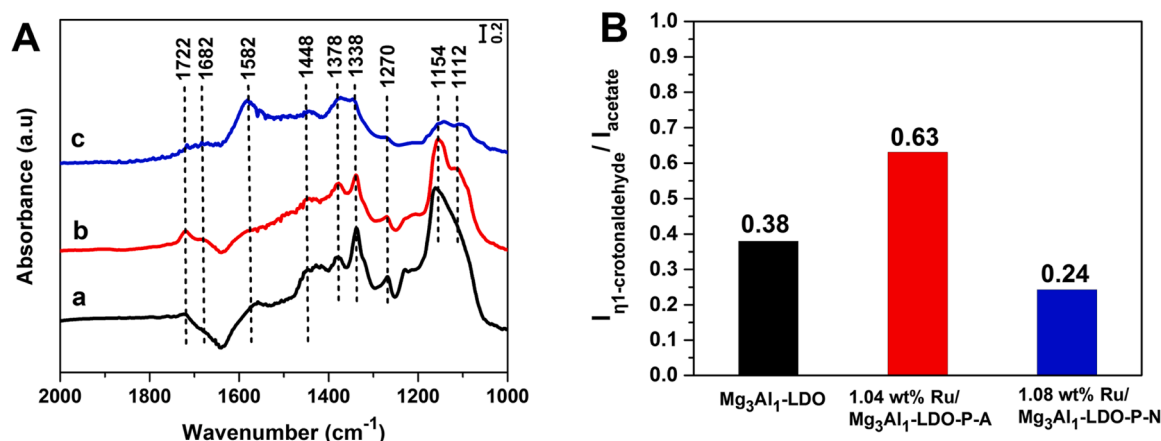


Fig. 6. (A) In-situ FT-IR spectra of acetaldehyde adsorption on (a) $\text{Mg}_3\text{Al}_1\text{-LDO}$, (b) 1.04 wt% Ru/ $\text{Mg}_3\text{Al}_1\text{-LDO-P-A}$, and (c) 1.08 wt% Ru/ $\text{Mg}_3\text{Al}_1\text{-LDO-P-N}$. (B) The relative intensity of $I_{\eta^1\text{-crotonaldehyde}} / I_{\text{acetate}}$ on $\text{Mg}_3\text{Al}_1\text{-LDO}$, 1.04 wt% Ru/ $\text{Mg}_3\text{Al}_1\text{-LDO-P-A}$, and 1.08 wt% Ru/ $\text{Mg}_3\text{Al}_1\text{-LDO-P-N}$.

predominates, while bidentate-adsorbed ethoxide at 1054 cm^{-1} become predominant on Ru supported $\text{Mg}_3\text{Al}_1\text{-LDO}$ (Fig. 5b and c), especially on LDO supported atomic Ru (Fig. 5b). This favored bidentate-adsorption of ethoxide is possible to result from the synergies between atomic Ru and basic sites on LDO surface. In the desorption with the temperature programmed from 50° to 400°C , the bands around 1436 and 1384 cm^{-1} from CH_2 and CH_3 group in adsorbed ethoxide vanishes along with other bands assigned to adsorbed ethoxide and acetaldehyde, and then the absorption assigned to $\text{OCO } \nu_s$ of adsorbed acetate emerges at 1436 cm^{-1} . On LDO supported atomic Ru or Ru nanoparticles, the bands around 1576 , 1436 and 1328 cm^{-1} , assigned to $\text{OCO } \nu_{\text{as}}$, $\text{OCO } \nu_s$ and $\text{CH}_3 \delta$ of adsorbed acetate (formation by $\alpha\text{-C-H}$ scission of acetaldehyde), are clearly observed over 200°C , indicating that Ru promotes the dehydrogenation. The adsorption as acetate makes it difficult to desorb and proceed the following condensation. The weaker intensity for acetate adsorption on atomic Ru than on the Ru nanoparticles (Fig. 5b and c) demonstrates the excellent ability of atomic Ru for condensation. The FT-IR results of ethanol adsorption-desorption well account for role of supported Ru, especially atomic Ru, in the adsorption, activation, and dehydrogenation of ethanol, consistent with the catalytic results (Table 2). On Ru nanoparticles, two additional bands are observed at 2032 and 1926 cm^{-1} , assigned to the adsorption of CO [32], with the desorption temperature increased over 150°C , indicative of the occurrence of decarbonylation on Ru nanoparticles. However, no adsorption

of CO can be found in the FT-IR spectra of ethanol adsorption-desorption on atomic Ru, indicating that no decarbonylation occurs. The FT-IR results explain why the catalysis of atomic Ru affords a carbon balance of 94% (Table 2, entry 2), while the catalysis of Ru nanoparticles affords a carbon balance of 72% (Table 2, entry 8) in the ethanol coupling to n-butanol. The lower carbon balance is caused by the decarbonylation of acetaldehyde.

The aldol condensation of acetaldehyde is a key step for the C–C bond formation. So in-situ FT-IR spectra of acetaldehyde adsorption on pristine support ($\text{Mg}_3\text{Al}_1\text{-LDO}$), atomic Ru (1.04 wt% Ru/ $\text{Mg}_3\text{Al}_1\text{-LDO-P-A}$), and Ru nanoparticles (1.08 wt% Ru/ $\text{Mg}_3\text{Al}_1\text{-LDO-P-N}$) has been recorded. As shown in Fig. 6A, the absorption bands around 1722 , 1682 , 1582 , 1448 , 1378 , 1338 , 1270 , 1154 , and 1112 cm^{-1} are observed in each case. According to previous reports [51–53], the band at 1722 cm^{-1} can be assigned to $\eta^1\text{-acetaldehyde}$ linear adsorption, the band at 1682 cm^{-1} can be assigned to the stretching vibration of C=O group ($\text{C=O } \nu$) in adsorbed crotonaldehyde, the bands at 1582 , 1448 , and 1338 cm^{-1} can be assigned to $\text{OCO } \nu_{\text{as}}$, $\text{OCO } \nu_s$ and $\text{CH}_3 \delta$ vibrations of adsorbed acetate (formation by $\alpha\text{-C-H}$ scission of acetaldehyde), the band at 1378 cm^{-1} can be assigned to the scissoring vibration of CH_3 group ($\text{CH}_3 \delta$) in adsorbed acetaldehyde, the bands at 1270 and 1154 cm^{-1} can be assigned to the stretching vibrations of C–O group ($\text{C–O } \nu$) and C–C group ($\text{C–C } \nu$) in $\eta^2\text{-adsorbed}$ acetaldehyde, and the band around 1112 cm^{-1} can be assigned to the scissoring vibration of C–C

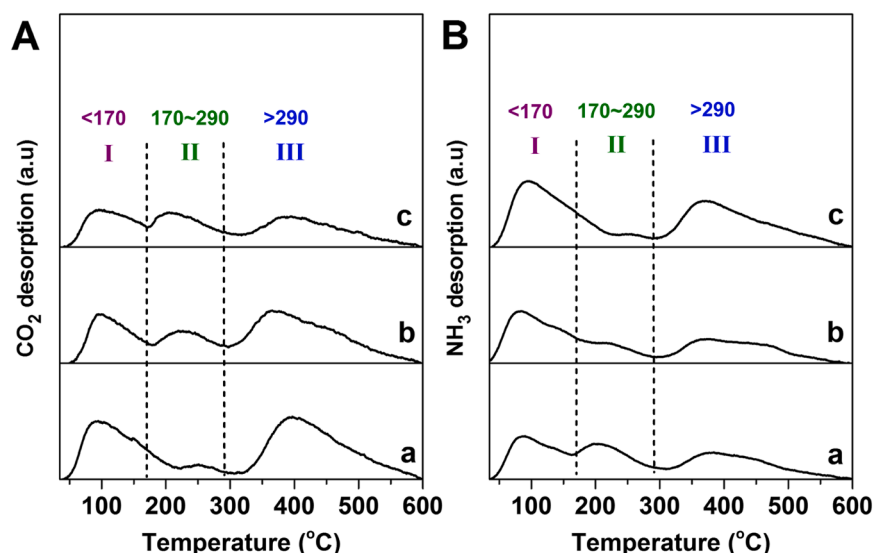


Fig. 7. (A) $\text{CO}_2\text{-TPD}$ profiles divided into several contributions corresponding to weak basic (I, purple), medium-strong basic (II, olive) and strong basic (III, blue) sites, for (a) 1.04 wt% Ru/ $\text{Mg}_3\text{Al}_1\text{-LDO-P-A}$, (b) 1.11 wt% Ru/ $\text{Mg}_3\text{Al}_{0.9}\text{Ga}_{0.1}\text{-LDO-P-A}$, and (c) 1.07 wt% Ru/ $\text{Mg}_3\text{Al}_{0.9}\text{Zr}_{0.1}\text{-LDO-P-A}$. (B) $\text{NH}_3\text{-TPD}$ profiles divided into several contributions corresponding to weak acidic (I, purple), medium-strong acidic (II, olive) and strong acidic (III, blue) sites, (a) 1.04 wt% Ru/ $\text{Mg}_3\text{Al}_1\text{-LDO-P-A}$, (b) 1.11 wt% Ru/ $\text{Mg}_3\text{Al}_{0.9}\text{Ga}_{0.1}\text{-LDO-P-A}$, and (c) 1.07 wt% Ru/ $\text{Mg}_3\text{Al}_{0.9}\text{Zr}_{0.1}\text{-LDO-P-A}$.

(C-C δ) group in adsorbed acetaldehyde. Compared to the pristine $\text{Mg}_3\text{Al}_2\text{LDO}$ (Fig. 6A, a), the η^1 -acetaldehyde linear adsorption at 1722 cm^{-1} , the absorption mode corresponding to less strongly bound species of acetaldehyde that easily carries on condensation [49], becomes more obvious on the atomic Ru supported $\text{Mg}_3\text{Al}_2\text{LDO}$ (Fig. 6A, b). Meanwhile, the relative intensity of the band for the stretching vibration of C=O group (C=O ν) in adsorbed crotonaldehyde at 1682 cm^{-1} to the band for the adsorbed acetate is observed more visible on atomic Ru than on $\text{Mg}_3\text{Al}_2\text{LDO}$ and Ru particles (Fig. 6B), consistent with selectivity to acetaldehyde condensation. Both pristine (Fig. 6A, a) and atomic Ru supported $\text{Mg}_3\text{Al}_2\text{LDO}$ (Fig. 6A, b) exhibit weaker absorption of η^2 -adsorbed acetaldehyde at 1154 cm^{-1} and stronger absorption of OCO ν_{as} at 1582 cm^{-1} than Ru particles supported $\text{Mg}_3\text{Al}_2\text{LDO}$ (Fig. 6A, c), indicating that η^2 -adsorption of acetaldehyde and formation of adsorbed acetate is disfavored on pristine and atomic Ru supported $\text{Mg}_3\text{Al}_2\text{LDO}$. Either the η^2 -adsorbed acetaldehyde, or the adsorbed acetate inhibits further condensation of acetaldehyde, well consistent with the lower selectivity of acetaldehyde (Table 2, entries 1–2 and 8) on supported Ru nanoparticles (1.08 wt% Ru/ $\text{Mg}_3\text{Al}_2\text{LDO-P-N}$) than on pristine $\text{Mg}_3\text{Al}_2\text{LDO}$ and $\text{Mg}_3\text{Al}_2\text{LDO}$ supported atomic Ru (1.04 wt% Ru/ $\text{Mg}_3\text{Al}_2\text{LDO-P-A}$). These results well account for the higher selectivity of n-butanol on atomic Ru supported $\text{Mg}_3\text{Al}_2\text{LDO}$ than on $\text{Mg}_3\text{Al}_2\text{LDO}$ itself (Table 2, entry 2 versus 1).

As mentioned above, the introduction of atomic Ru also increases the population of Al_{IV} species on $\text{Mg}_3\text{Al}_2\text{LDO}$. So the selectivity to acetaldehyde condensation products has been correlated as a function of the population of Al_{IV} species. The selectivity to the acetaldehyde condensation products increases with the population of Al_{IV} species (Fig. S7, b). But the 83.4% of selectivity to acetaldehyde condensation products on atomic Ru supported $\text{Mg}_3\text{Al}_2\text{LDO}$ is 12.2% higher than the selectivity predicted only through correlating the selectivity to acetaldehyde condensation products with the population of Al_{IV} species, implying that besides atomic Ru itself, the Al_{IV} species or even the synergy between Al_{IV} species and atomic Ru could also contribute to the acetaldehyde condensation.

3.4. Acid-base properties and ethanol coupling

Ga (III) or Zr (IV) containing LDO has been further used to support atomic Ru to investigate the effects of surface acidic and basic properties on ethanol coupling. The surface basicity and acidity of LDO-supported atomic Ru have been determined by CO_2 -TPD and NH_3 -TPD technique (Fig. 7) and the data are presented in Table S1 and S2. The CO_2 -TPD profiles (Fig. 7A) can be divided [54] into three contributions: weak ($< 170^\circ\text{C}$), medium-strong (170 – 290°C), and strong ($> 290^\circ\text{C}$) basic sites. The introduction of Ga (III) or Zr (IV) has no obvious effects on total number of basic sites, with decreased amount of weak basic sites, increased amount of medium-strong basic sites, and unchanged amount of strong basic sites (Table S1). The NH_3 -TPD profiles (Fig. 7B) can be divided [55] into three contributions: weak ($< 170^\circ\text{C}$), medium-strong (170 – 290°C), and strong ($> 290^\circ\text{C}$) acidic sites. The introduction of Ga (III) or Zr (IV) increases the amount of weak acidic sites, decreases the amount of medium-strong acidic sites, and increases the amount of strong acidic sites (Table S2). As a result, total number of acidic sites increases, especially with the introduction of Zr (IV). The acidic type (Brønsted or Lewis acidic sites) have been determined by FT-IR spectra of pyridine adsorption. As shown in Fig. S13, the band characteristic of pyridine adsorption on Lewis acidic sites at 1441 – 1446 cm^{-1} is clearly observed in each case [56], without the band typical of Brønsted acidic sites around 1540 cm^{-1} resolved. Applied in the ethanol coupling to butanol (Table 2, entries 10–11), it is not surprising that the intermolecular dehydration is promoted with increasing number of acidic sites. From the selectivity of acetaldehyde condensation products or ethanol dehydration product, i.e. diethyl ether, as a function of acidic sites (Fig. S14), it can be seen that either weak or strong acidic sites favor ethanol dehydration while medium-strong acidic sites favor

acetaldehyde condensation.

Ethanol coupling to C_{4+} alcohols has been proposed to follow several steps including mainly ethanol dehydrogenation and acetaldehyde condensation. In order to investigate which step is more susceptible to active sites in the pathway of ethanol coupling to C_{4+} alcohols on atomic Ru (1.04 wt% Ru/ $\text{Mg}_3\text{Al}_2\text{LDO-P-A}$), WHSV has been varied and correlated to ethanol conversion (Fig. S15, a). With WHSV increasing gradually from 3.2 h^{-1} to 9.6 h^{-1} , the ethanol conversion decreasing monotonically from 29.6% to 9.8% (Fig. S15, a) while the ethanol converted in gram on per gram of catalyst keep constant ($\sim 0.95\text{ h}^{-1}$). Almost no obvious changes in the selectivity to diethyl ether ($\sim 0.068\text{ h}^{-1}$) are observed, suggesting that 0.882 h^{-1} of acetaldehyde is obtained. The actual acetaldehyde detected increase from 0.057 h^{-1} to 0.099 h^{-1} (Fig. S15, b), indicating that the acetaldehyde conversion decreases from 0.825 h^{-1} to 0.783 h^{-1} . As a result, the obtained n-butanol and C_{4+} alcohols decrease from 0.666 h^{-1} to 0.641 h^{-1} and from 0.785 h^{-1} to 0.698 h^{-1} (Fig. S15, b). These results clearly demonstrate the ethanol dehydrogenation is not susceptible due to the high dehydrogenation activity of atomic Ru, further showing the advantage of Ru in dehydrogenation. It is interesting that acetaldehyde condensation is depressed more obviously by increasing WHSV than ethanol dehydrogenation (Fig. S15, b), indicating that ethanol dehydrogenation has advantages over acetaldehyde condensation on $\text{Mg}_3\text{Al}_2\text{LDO}$ supported atomic Ru.

4. Conclusions

In summary, atomic Ru catalysis for ethanol coupling to C_{4+} alcohols have been investigated using LDO as the support in this work. It has been demonstrated that atomic Ru supported on $\text{Mg}_3\text{Al}_2\text{LDO}$ remarkably promotes the coupling of ethanol, achieving a selectivity of 82.6% to C_{4+} alcohols under an ethanol conversion of 29.6%. Atomic promotes ethanol dehydrogenation and the following aldol condensation of acetaldehyde. Atomic Ru catalysis build a bridge between homogeneous and heterogeneous catalytic strategies for ethanol coupling, which is expected to be further applied in the coupling reaction of other alcohols.

CRedit authorship contribution statement

Bowen Yuan: Conceptualization, Formal analysis, Investigation, Data curation, Writing – original draft, Writing – review & editing, Visualization. **Jian Zhang:** Formal analysis, Validation, Investigation, Data curation, Writing – review & editing. **Zhe An:** Validation, Investigation. **Yanru Zhu:** Validation, Investigation. **Xin Shu:** Investigation. **Hongyan Song:** Investigation. **Xu Xiang:** Investigation. **Wanning Wang:** Investigation. **Yusheng Jing:** Data curation. **Lirong Zheng:** Formal analysis, Investigation, Resources, Supervision. **Jing He:** Conceptualization, Validation, Formal analysis, Investigation, Project administration, Writing – review & editing, Supervision, Funding acquisition.

Declaration of Competing Interest

The authors declare no competing financial interest.

Acknowledgements

Financial support by National Natural Science Foundation of China (21521005 and 22138001), the National Key R&D Program of China (2017YFA0206804), and the Fundamental Research Funds for the Central Universities (XK1802-6) is gratefully acknowledged. We thank Prof. Song Hong from Beijing University of Chemical Technology for his help in Ac-HAADF-STEM characterization.

Appendix A. Supporting information

Supplementary data associated with this article can be found in the online version at [doi:10.1016/j.apcatb.2022.121271](https://doi.org/10.1016/j.apcatb.2022.121271).

References

- [1] P. Fairley, Introduction: next generation biofuels, *Nature* 474 (2011) S2–S5.
- [2] N. Savage, Fuel options: the ideal biofuel, *Nature* 474 (2011) S9–S11.
- [3] J.T. Kozlowski, R.J. Davis, Heterogeneous catalysts for the Guerbet coupling of alcohols, *ACS Catal.* 3 (2013) 1588–1600.
- [4] J. Würtz, G. Schnabel, G. Frisch, Surfactant/solvent systems, *US Pat.* 7615232, 2009.
- [5] S. Hoshiyama, H. Muto, S. Shinke, K. Otsuka, S. Takigawa, H. Yamazaki, Process for producing an alcohol by hydroformylation, *US Pat.* 4447661, 1984.
- [6] G.R. Dowson, M.F. Haddow, J. Lee, R.L. Wingad, D.F. Wass, Catalytic conversion of ethanol into an advanced biofuel: Unprecedented selectivity for n-butanol, *Angew. Chem. Int. Ed.* 52 (2013) 9005–9008.
- [7] R.L. Wingad, P.J. Gates, S.T.G. Street, D.F. Wass, Catalytic conversion of ethanol to n-butanol using ruthenium P-N ligand complexes, *ACS Catal.* 5 (2015) 5822–5826.
- [8] T.A. DiBenedetto, W.D. Jones, Upgrading of ethanol to n-butanol via a ruthenium catalyst in aqueous solution, *Organometallics* 40 (2021) 1884–1888.
- [9] H. Aitchison, R.L. Wingad, D.F. Wass, Homogeneous ethanol to butanol catalysis-Guerbet renewed, *ACS Catal.* 6 (2016) 7125–7132.
- [10] K.N. Tseng, S. Lin, J.W. Kampf, N.K. Szymczak, Upgrading ethanol to 1-butanol with a homogeneous air-stable ruthenium catalyst, *Chem. Commun.* 52 (2016) 2901–2904.
- [11] Y. Xie, Y. Ben-David, L.J. Shimon, D. Milstein, Highly efficient process for production of biofuel from ethanol catalyzed by ruthenium pincer complexes, *J. Am. Chem. Soc.* 138 (2016) 9077–9080.
- [12] K. Koda, T. Matsu-ura, Y. Obora, Y. Ishii, Guerbet reaction of ethanol to n-butanol catalyzed by iridium complexes, *Chem. Lett.* 38 (2009) 838–839.
- [13] G. Xu, T. Lammens, Q. Liu, X. Wang, L. Dong, A. Caiazzo, N. Ashraf, J. Guan, X. Mu, Direct self-condensation of bio-alcohols in the aqueous phase, *Green Chem.* 16 (2014) 3971–3977.
- [14] S. Chakraborty, P.E. Piszal, C.E. Hayes, R.T. Baker, W.D. Jones, Highly selective formation of n-butanol from ethanol through the Guerbet process: a tandem catalytic approach, *J. Am. Chem. Soc.* 137 (2015) 14264–14267.
- [15] S. Fu, Z. Shao, Y. Wang, Q. Liu, Manganese-catalyzed upgrading of ethanol into 1-butanol, *J. Am. Chem. Soc.* 139 (2017) 11941–11948.
- [16] J. Sun, Y. Wang, Recent advances in catalytic conversion of ethanol to chemicals, *ACS Catal.* 4 (2014) 1078–1090.
- [17] A. Ndou, Dimerisation of ethanol to butanol over solid-base catalysts, *Appl. Catal. A* 251 (2003) 337–345.
- [18] C. Yang, Z.Y. Meng, Bimolecular condensation of ethanol to 1-butanol catalyzed by alkali cation zeolites, *J. Catal.* 142 (1993) 37–44.
- [19] M. León, E. Díaz, S. Ordóñez, Ethanol catalytic condensation over Mg-Al mixed oxides derived from hydrotalcites, *Catal. Today* 164 (2011) 436–442.
- [20] D.L. Carvalho, R.R. de Avillez, M.T. Rodrigues, L.E.P. Borges, L.G. Appel, Mg and Al mixed oxides and the synthesis of n-butanol from ethanol, *Appl. Catal. A* 415–416 (2012) 96–100.
- [21] T. Tsuchida, S. Sakuma, T. Takeguchi, W. Ueda, Direct synthesis of n-butanol from ethanol over nonstoichiometric hydroxyapatite, *Ind. Eng. Chem. Res.* 45 (2006) 8634–8642.
- [22] T. Tsuchida, J. Kubo, T. Yoshioka, S. Sakuma, T. Takeguchi, W. Ueda, Reaction of ethanol over hydroxyapatite affected by Ca/P ratio of catalyst, *J. Catal.* 259 (2008) 183–189.
- [23] S. Ogo, A. Onda, K. Yanagisawa, Selective synthesis of 1-butanol from ethanol over strontium phosphate hydroxyapatite catalysts, *Appl. Catal. A* 402 (2011) 188–195.
- [24] S. Ogo, A. Onda, Y. Iwasa, K. Hara, A. Fukuoaka, K. Yanagisawa, 1-Butanol synthesis from ethanol over strontium phosphate hydroxyapatite catalysts with various Sr/P ratios, *J. Catal.* 296 (2012) 24–30.
- [25] J.H. Earley, R.A. Bourne, M.J. Watson, M. Poliakoff, Continuous catalytic upgrading of ethanol to n-butanol and >C4 products over Cu/CeO₂ catalysts in supercritical CO₂, *Green Chem.* 17 (2015) 3018–3025.
- [26] D. Jiang, X. Wu, J. Mao, J. Ni, X. Li, Continuous catalytic upgrading of ethanol to n-butanol over Cu-CeO₂/AC catalysts, *Chem. Commun.* 52 (2016) 13749–13752.
- [27] Z. Sun, A. Couto Vasconcelos, G. Bottari, M.C.A. Stuart, G. Bonura, C. Cannilla, F. Frusteri, K. Barta, Efficient catalytic conversion of ethanol to 1-butanol via the Guerbet reaction over copper- and nickel-doped porous, *ACS Sustain. Chem. Eng.* 5 (2016) 1738–1746.
- [28] C. Lopez-Olmos, M.V. Morales, A. Guerrero-Ruiz, C. Ramirez-Barria, E. Asedegbega-Nieto, I. Rodriguez-Ramos, Continuous gas-phase condensation of bioethanol to 1-butanol over bifunctional Pd/Mg and Pd/Mg-carbon catalysts, *ChemSusChem* 11 (2018) 3502–3511.
- [29] D. Jiang, G. Fang, Y. Tong, X. Wu, Y. Wang, D. Hong, W. Leng, Z. Liang, P. Tu, L. Liu, K. Xu, J. Ni, X. Li, Multifunctional Pd@UiO-66 catalysts for continuous catalytic upgrading of ethanol to n-butanol, *ACS Catal.* 8 (2018) 11973–11978.
- [30] J. Pang, M. Zheng, L. He, L. Li, X. Pan, A. Wang, X. Wang, T. Zhang, Upgrading ethanol to n-butanol over highly dispersed Ni-MgAlO catalysts, *J. Catal.* 344 (2016) 184–193.
- [31] J. Zhang, K. Shi, Z. An, Y. Zhu, X. Shu, H. Song, X. Xiang, J. He, Acid-base promoted dehydrogenation coupling of ethanol on supported Ag particles, *Ind. Eng. Chem. Res.* 59 (2020) 3342–3350.
- [32] J. Quesada, L. Faba, E. Díaz, S. Ordóñez, Enhancement of the 1-butanol productivity in the ethanol condensation catalyzed by noble metal nanoparticles supported on Mg-Al mixed oxide, *Appl. Catal. A* 563 (2018) 64–72.
- [33] J. Pang, M. Zheng, T. Zhang, Chapter-two-synthesis of ethanol and its catalytic conversion, *Adv. Catal.* 64 (2019) 89–191.
- [34] J. Pang, M. Yin, P. Wu, X. Li, H. Li, M. Zheng, T. Zhang, Advances in catalytic dehydrogenation of ethanol to acetaldehyde, *Green Chem.* 23 (2021) 7902–7916.
- [35] T. Bligaard, J.K. Nørskov, S. Dahl, J. Matthiesen, C.H. Christensen, J. Sehested, The Brønsted-Evans-Polanyi relation and the volcano curve in heterogeneous catalysis, *J. Catal.* 224 (2004) 206–217.
- [36] F. Cavani, F. Trifiro, A. Vaccari, Hydrotalcite-type anionic clays: preparation, properties and applications, *Catal. Today* 11 (1991) 173–301.
- [37] K. Mori, T. Taga, H. Yamashita, Isolated single-atomic Ru catalyst bound on a layered double hydroxide for hydrogenation of CO₂ to formic acid, *ACS Catal.* 7 (2017) 3147–3151.
- [38] B. Ravel, M. Newville, ATHENA, ARTEMIS, HEPHAESTUS: data analysis for X-ray absorption spectroscopy using IFEFFIT, *J. Synchrotron Rad.* 12 (2005) 537–541.
- [39] H. Funke, A.C. Scheinost, M. Chukalina, Wavelet analysis of extended X-ray absorption fine structure data, *Phys. Rev. B* 71 (2005), 094110.
- [40] H. Funke, M. Chukalina, A.C. Scheinost, A new FEFF-based wavelet for EXAFS data analysis, *J. Synchrotron Rad.* 14 (2007) 426–432.
- [41] D.E. Mears, Tests for transport limitations in experimental catalytic reactors, *Ind. Eng. Chem. Process Des. Dev.* 10 (1971) 541–547.
- [42] P.B. Weisz, C.D. Prater, Interpretation of measurements in experimental catalysis, *Adv. Catal.* 6 (1954) 143–196.
- [43] S.Y. Chin, C.T. Williams, M.D. Amiridis, FTIR studies of CO adsorption on Al₂O₃- and SiO₂-supported Ru catalysts, *J. Phys. Chem. B* 110 (2006) 871–882.
- [44] J. Zhang, B. Ge, T. Liu, Y. Yang, B. Li, W. Li, Robust ruthenium-saving catalyst for high-temperature carbon dioxide reforming of methane, *ACS Catal.* 10 (2020) 783–791.
- [45] P. Li, M. Wang, X. Duan, L. Zheng, X. Cheng, Y. Zhang, Y. Kuang, Y. Li, Q. Ma, Z. Feng, W. Liu, X. Sun, Boosting oxygen evolution of single-atomic ruthenium through electronic coupling with cobalt-iron layered double hydroxides, *Nat. Commun.* 10 (2019) 1711.
- [46] V. Sreeja, T.S. Smitha, D. Nand, T.G. Ajithkumar, P.A. Joy, Size dependent coordination behavior and cation distribution in MgAl₂O₄ nanoparticles from ²⁷Al solid state NMR studies, *J. Phys. Chem. C* 112 (2008) 14737–14744.
- [47] C. Elmasides, D.I. Kondarides, W. Grünert, X.E. Verykios, XPS and FTIR study of Ru/Al₂O₃ and Ru/TiO₂ catalysts: reduction characteristics and interaction with a methane-oxygen mixture, *J. Phys. Chem. B* 103 (1999) 5227–5239.
- [48] D. Li, R. Li, M. Lu, X. Lin, Y. Zhan, L. Jiang, Carbon dioxide reforming of methane over Ru catalysts supported on Mg-Al oxides: a highly dispersed and stable Ru/Mg (Al)O catalyst, *Appl. Catal. B* 200 (2017) 566–577.
- [49] J.V. Ochoa, C. Trevisanut, J.-M.M. Millet, G. Busca, F. Cavani, In situ DRIFTS-MS study of the anaerobic oxidation of ethanol over spinel mixed oxides, *J. Phys. Chem. C* 117 (2013) 23908–23918.
- [50] M. Li, Z. Wu, S.H. Overbury, Surface structure dependence of selective oxidation of ethanol on faceted CeO₂ nanocrystals, *J. Catal.* 306 (2013) 164–176.
- [51] A.K.P. Mann, Z. Wu, F.C. Calaza, S.H. Overbury, Adsorption and reaction of acetaldehyde on shape-controlled CeO₂ nanocrystals: elucidation of structure-function relationships, *ACS Catal.* 4 (2014) 2437–2448.
- [52] S. Bhasker-Ranganath, M.S. Rahman, C. Zhao, F. Calaza, Z. Wu, Y. Xu, Elucidating the mechanism of ambient-temperature aldol condensation of acetaldehyde on ceria, *ACS Catal.* 11 (2021) 8621–8634.
- [53] W.E. Taifan, G.X. Yan, J. Baltrusaitis, Surface chemistry of MgO/SiO₂ catalyst during the ethanol catalytic conversion to 1,3-butadiene: in-situ DRIFTS and DFT study, *Catal. Sci. Technol.* 7 (2017) 4648–4668.
- [54] J. Zhang, W. Yan, Z. An, H. Song, J. He, Interface-promoted dehydrogenation and water-gas shift toward high-efficient H₂ production from aqueous phase reforming of cellulose, *ACS Sustain. Chem. Eng.* 6 (2018) 7313–7324.
- [55] W. Liu, J. Sun, X. Zhang, M. Wei, Supported Ag catalysts on Mg-Al oxides toward oxidant-free dehydrogenation reaction of benzyl alcohol, *Ind. Eng. Chem. Res.* 57 (2018) 15606–15612.
- [56] A. Penkova, L.F. Bobadilla, F. Romero-Sarria, M.A. Centeno, J.A. Odriozola, Pyridine adsorption on NiSn/MgO–Al₂O₃: an FTIR spectroscopic study of surface acidity, *Appl. Surf. Sci.* 317 (2014) 241–251.